Kalthoff, N., Adler, B., Wieser, A., Kohler, M., Träumner, K., Handwerker, J., Corsmeier, U., Khodayar, S., Lambert, D., Kopmann, A., Kunka, N., Dick, G., Ramatschi, M., Wickert, J., Kottmeier, C. (2013): KITcube – a mobile observation platform for convection studies deployed during HyMeX. - *Meteorologische Zeitschrift*, *22*, 6, 633-647

DOI: 10.1127/0941-2948/2013/0542

Meteorologische Zeitschrift, Vol. 22, No. 6, 633–647 (February 2014)

Open Access Article

KITcube – a mobile observation platform for convection studies deployed during HyMeX

Norbert Kalthoff[1,*], Bianca Adler[1], Andreas Wieser[1], Martin Kohler[1], Katja Träumner[1], Jan Handwerker[1], Ulrich Corsmeier[1], Samiro Khodayar[1], Dominique Lambert[2], Andreas Kopmann[3], Norbert Kunka[3], Galina Dick[4], Markus Ramatschi[4], Jens Wickert[4] and Christoph Kottmeier[1]

[1]Institut für Meteorologie und Klimaforschung (IMK-TRO), Karlsruher Institut für Technologie (KIT), Karlsruhe, Germany
[2]Laboratoire d'Aérologie, Université de Toulouse, Toulouse, France
[3]Institut für Prozessverarbeitung und Elektronik (IPE), Karlsruher Institut für Technologie (KIT), Karlsruhe, Germany
[4]Department of Geodesy and Remote Sensing, German Research Centre for Geosciences (GFZ), Potsdam, Germany

(Manuscript received August 9, 2013; in revised form October 2, 2013; accepted October 3, 2013)

Abstract

With the increase of spatial resolution of weather forecast models to order O(1 km), the need for adequate observations for model validation becomes evident. Therefore, we designed and constructed the "KITcube", a mobile observation platform for convection studies of processes on the meso-γ scale. The KITcube consists of in-situ and remote sensing systems which allow measuring the energy balance components of the Earth's surface at different sites; the mean atmospheric conditions by radiosondes, GPS station, and a microwave radiometer; the turbulent characteristics by a sodar and wind lidars; and cloud and precipitation properties by use of a cloud radar, a micro rain radar, disdrometers, rain gauges, and an X-band rain radar. The KITcube was deployed fully for the first time on the French island of Corsica during the HyMeX (Hydrological cycle in the Mediterranean eXperiment) field campaign in 2012. In this article, the components of KITcube and its implementation on the island are described. Moreover, results from one of the HyMeX intensive observation periods are presented to show the capabilities of KITcube.

Keywords: HyMeX, convection, observation platform.

1 Introduction

During the last years, spatial resolution of weather forecast models increased to order O (1 km) allowing to resolve larger convective systems like thunderstorms. Convection, however, encompasses multiple scales from micro- to mesoscale. Therefore, the transition from convection initiation via shallow to deep convection is not simulated properly (Bryan et al., 2003). Besides, understanding of processes and mechanisms governing the convection development has been limited up to now.

To improve the knowledge about convection, scale-adapted measurements were performed (Weckwerth et al., 2004; Wilson and Roberts, 2006; Browning et al., 2007; Kottmeier et al., 2008; Wulfmeyer et al., 2011). So-called supersites were installed, where coordinated measurements of different in-situ and remote systems were exploited synergetically so that convective processes could be analysed (e.g. Miller and Slingo, 2007; Behrendt et al., 2011; Corsmeier et al., 2011; Kalthoff et al., 2013). Often, smaller-scale meteorological networks were embedded in larger-scale investigation domains to capture spatial inhomogeneities. Aircraft missions, including dropsonde releases, were performed to flexibly respond to convection evolution.

From these and previous observations, it was found that convection in many cases was initiated by low-level convergence zones (Khodayar et al., 2010; 2013) and favoured by small-scale moisture variability (Weckwerth, 2000). Convergence zones are often generated by mesoscale surface heterogeneities, e.g. given soil moisture (Taylor et al., 2011) and land-sea contrast or orography (Kalthoff et al., 2009). Besides triggering, convergence zones also support continued growth of convection because of the permanent upward motion and moisture transport there. For mountainous terrain, additional types of thunderstorm initiation mechanisms were distinguished (e.g. Banta, 1990): direct orographic lifting and obstacle or aerodynamic effects (blocking, flow deflection, gravity wave effects). The influence of islands on the triggering of thunderstorms was also documented well (e.g. Wilson et al., 2001; Qian, 2007). Mountainous islands turned out to be most effective, because sea breezes and valley winds that are roughly

*Corresponding author: Norbert Kalthoff, Institut für Meteorologie und Klimaforschung (IMK-TRO), Karlsruher Institut für Technologie (KIT), POB 3640, 76021 Karlsruhe, Germany, e-mail: norbert.kalthoff@kit.edu

DOI 10.1127/0941-2948/2013/0542
0941-2948/2013/0542 $ 6.75

in phase with each other may combine to strengthen the diurnal cycle of winds and form convergence zones during daytime (KOTTMEIER et al., 2000).

The "KITcube" was developed for state-of-the-art observations, the objective being to contribute to the understanding of the process chain from convection initiation via cloud formation to precipitation. It is a mobile observation platform consisting of various in-situ and remote sensing systems. Most of the measurement devices are preferably concentrated at one supersite. Additional instruments are distributed within an area of meso-γ scale extension to exploit the synergy of complementary measurements and to cover the spatial extension of convection-related phenomena. KITcube was implemented first during the international project HyMeX (Hydrological cycle in the Mediterranean eXperiment; DROBINSKI et al., 2014; DUCROCQ et al., 2013) on the French island of Corsica in the Mediterranean.

During the late summer and autumn, the western Mediterranean is often affected by heavy precipitation (DUCROCQ et al., 2008), mainly convective in nature (DOSWELL et al., 1998). Both the orography and the sea surface influence the formation and evolution of the convective systems in the region (HOMAR et al., 1999; BUZZI and FOSCHINI, 2000; ROTUNNO and FERRETTI, 2001). To improve the understanding of the initiation and development of heavy precipitation events in the Mediterranean region, the HyMeX project was initiated. Under this project, a special observation period (SOP) was conducted in autumn 2012 to provide comprehensive data sets for process studies and model evaluation alike. Due to the processes involved in convective precipitation, observations on different scales were carried out. During the SOP, the KITcube was positioned at one of HyMeX's supersites on the Corsican Island (Fig. 1).

Two main scientific goals were pursued with the deployment of KITcube at this position. (i) Corsica unites both features necessary to cause orographically induced convection or to modify it, i.e. a landmass of sufficient size (about 80 km by 180 km) and a high mountain ridge of up to 2700 m above mean sea level (MSL). The KITcube investigated the influence of the island on initiation and modification of isolated convection. (ii) For most of the synoptic conditions, under which severe precipitation events occur in the Ligurian Sea, the Corsican Island is on the upwind side (LAMBERT et al., 2011). Thus, KITcube was well-positioned to provide upstream conditions for the intense precipitation events affecting continental south-eastern France and northern and central Italy.

The aim of this paper is to introduce the KITcube observation platform, present its deployment on Corsica during the HyMeX field campaign in 2012, and to demonstrate its observation capabilities to investigate convective processes. For the latter, a time section from the intense observation period (IOP) 12a (11 October, 2012) was selected.

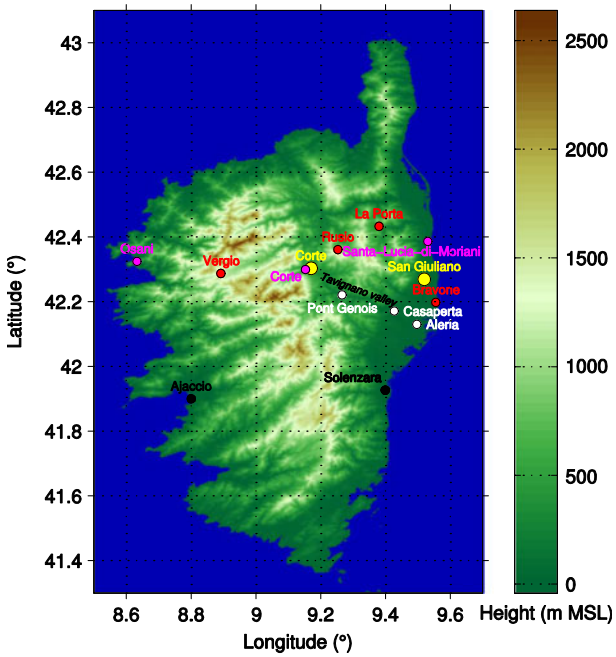

Figure 1: Deployment of KITcube devices on the Corsican Island: main deployment sites (yellow), mobile towers (white), GPS stations operated by IGN and ACTIPLAN (magenta), and additional GPS stations deployed by GFZ (red). For details see section 3.

2 The mobile observation platform KITcube

KITcube consists of measurement systems which provide information about the energy exchange at the surface, turbulence and mean conditions in the convective boundary layer (CBL) and whole troposphere, respectively, and about cloud and precipitation properties. The different measurement systems of KITcube are listed in Table 1, including e.g. temporal resolutions and measurement ranges of the main derived parameters. Details are given below.

2.1 Surface energy exchange and near-surface observations

The energy balance stations measure meteorological variables (temperature, humidity, wind speed and direction, air pressure, precipitation); radiation temperature of the surface; solar and reflected irradiance; long-wave incoming and outgoing radiation; soil heat, sensible heat, latent heat and momentum fluxes (KALTHOFF et al., 2006); as well as the moisture and temperature in the soil. The turbulent fluxes are measured with an ultrasonic anemometer/thermometer and a fast infrared hygrometer. For post-processing of turbulent fluxes, the eddy-correlation software package TK3.1 described by MAUDER and FOKEN (2011) is used.

Seven additional flux stations provide temperature, humidity (both at three levels), wind speed and wind

direction, momentum and sensible heat fluxes. The stations deliver information on the spatial variability of the sensible heat fluxes. Additionally, a scintillometer (SLS20, Scintec) measures the sensible heat flux for spatial averages along the laser beam with an averaging time of 1 minute. The transmitting laser beam and receiver are typically separated by a distance of about 100 m to 200 m.

A 20 m high meteorological tower provides wind speed, temperature, and humidity profiles as well as wind direction, and sensible heat and momentum fluxes at 20 m above ground level (AGL). Soil temperatures are measured at six different depths.

Battery-powered mobile towers that are deployed flexibly in the investigation area measure temperature, humidity, wind speed and wind direction, air pressure, precipitation, and sensible heat and momentum fluxes.

2.2 Mean and turbulent atmospheric conditions

To obtain vertical profiles of temperature, humidity, wind speed, and wind direction in the troposphere, two radiosonde systems (DFM-09, Graw) are available. Depending on height, the 1 s raw data are averaged over 2 s (between ground and 3 km AGL), 4 s (3 km and 10 km), and 8 s (> 10 km). During IOPs radiosondes are typically launched at 2- to 3-hour intervals. The sounding data are also used to derive significant levels and convection-related parameters, such as the convective condensation level (CCL), lifting condensation layer (LCL), level of free convection (LFC), convective inhibition (CIN), and convective available potential energy (CAPE).

A ground-based scanning microwave radiometer (humidity and temperature profiler, HATPRO) designed by Radiometer Physics measures the sky brightness temperature at 12 frequencies distributed within the 22-30 GHz and 51-59 GHz bands. With statistical retrievals provided by the University of Cologne (Löhnert and Crewell, 2003; Crewell and Löhnert, 2003), these sky brightness temperatures are inverted to obtain temperature and humidity profiles up to 10 km height. Using additional boundary layer scans, vertical temperature profiles are obtained in 50 m steps close to the surface and in steps of 200 m to 400 m in the free troposphere. The system also provides integrated water vapour (IWV) and liquid water path (LWP) data along the line of sight. 360° azimuth scans at fixed elevation angles carried out on a regular basis provide information about spatial humidity distribution. The temperature of cloud base is determined with an upwards directed infrared thermometer.

Additionally, a JAVAD GPS receiver combined with surface observations of temperature and pressure is used to determine IWV with a temporal resolution of 15 min. The calculations are performed by GFZ Potsdam based on algorithms described by Dick et al. (2001) and Gendt et al. (2004).

To determine the mean horizontal and vertical velocity and vertical velocity variance, a phased array sodar (MFAS, Scintec) is used. Operation frequencies in the 2 kHz band and multi-frequency operation allow for a spatial resolution of 10 m and a maximum measurement range of up to 1000 m AGL. Backscatter data can be used for mixing height detection.

One 2 µm and another 1.6 µm heterodyne wind lidar with beam width of 75 mm at laser exit (WindTracer, Lockheed Martin) are part of KITcube to measure aerosol backscatter and calculate radial velocity (Träumner et al., 2011). Applying the vertical stare mode immediately yields vertical velocity with a time resolution of 1 s from about 375 m AGL to the top of the boundary layer and partly above (depending on the aerosol concentration). The measurements are mainly restricted to the cloud-free atmosphere, because wind lidars only partly penetrate clouds. The uncorrelated noise of velocity could be estimated to be less than 0.2 m s^{-1} for a high signal to noise ratio (SNR) range. Both lidars have two-axis scanners and yield profiles of the horizontal wind velocity via the velocity-azimuth display (VAD) technique (e.g. Browning and Wexler, 1968). Synchronised monitoring of the two lidars allow for dual-Doppler measurements (Stawiarski et al., 2013). The CBL depth can be estimated using the profiles of the vertical velocity variance.

In order to cover the range between the surface and the lowest WindTracer measurement heights, a third wind lidar (Windcube 8, Leosphere) with a wavelength of 1.54 µm is used, which measures the wind profile from 40 m AGL up to about 600 m AGL with averaging times of 1.6 s to 10 min and a vertical range resolution of 20 m. In normal operation mode, this small wind lidar has a fixed elevation angle of 75.2° and an azimuth scanner. By means of a 4-point stop and stare plane position indicator (PPI) scan applying the VAD algorithm, the wind profile is calculated. Running a special operation mode by using a motorised tilted table allows for continuous vertical stare measurements for the direct detection of vertical velocity. In combination with a WindTracer, this leads to a full vertical coverage of vertical velocity from the ground up into the entrainment zone.

2.3 Measurements of clouds and precipitation properties

Clouds and precipitation properties are measured by remote sensing techniques as well as by in-situ observations. Every two minutes, two cameras with fish eye lenses take photos of the upper hemisphere, from which the cloud type and cloud cover can be estimated.

A 35.5 GHz scanning cloud radar (MIRA36-S, Metek) is implemented in the KITcube to measure cloud

Table 1a: Measurement systems included in KITcube and main derived parameters, typical settings, and measurement ranges of instruments.

Device (Manufacturer)	Quantity	Derived parameters	Temporal resolution of derived parameters (raw data)	Measurement heights (m AGL)
		Surface energy exchange and near-surface observations		
Energy balance stations (Different manufacturers)	2	Temperature	10 min (1 s)	3
		Humidity	10 min (1 s)	3
		3-d wind	10 min (0.05 s)	4
		Humidity	10 min (0.05 s)	4
		Temperature	10 min (0.05 s)	4
		Air pressure	10 min (1 s)	0.1
		Precipitation	10 min	1
		Radiation temperature of surface	10 min (1 s)	0
		Solar and reflected irradiance	10 min (1 s)	3
		Long wave incoming and outgoing radiation	10 min (1 s)	3
		Sensible and latent heat and momentum fluxes	30 min (0.05 s)	4
		Soil heat flux	10 min (1 s)	−0.05
		Soil moisture	10 min	4 variable depths
		Soil temperature	10 min	4 variable depths
Flux stations (Different manufacturers)	7	Temperature	10 min (1 s)	1, 2, 4
		Humidity	10 min (1 s)	1, 2, 4
		3-d wind	10 mm (0.05 s)	5
		Temperature	10 min (0.05 s)	5
		Air pressure	10 min (1 s)	0.1
		Sensible heat and momentum fluxes	30 min (0.05 s)	5
Scintillometer (Scintec)	1	Sensible heat flux	1 min	2–3
20-m tower (Different manufacturers)	1	Temperature	10 min (1 s)	0.5, 1, 2, 4, 8, 16, 19
		Humidity	10 min (1 s)	0.5, 1, 2, 4, 8, 16, 19
		Wind speed	10 min (1 s)	0.5, 1, 2, 4, 8, 16, 19
		Wind direction	10 min (1 s)	20
		Temperature	10 min (0.05 s)	20
		Soil temperature	10 min (1 s)	0.02, 0.04, 0.08, 0.16, 0.32, 0.64
		3-d wind	10 min (0.05 s)	20
		Sensible heat and momentum fluxes	30 min (0.05 s)	20
Mobile towers (Young)	3	Temperature	10 min	2
		Humidity	10 min	2
		3-d wind	0.03 s	4
		Temperature	0.03 s	4
		Air pressure	10 min	1
		Precipitation	10 min	1
		Sensible heat and momentum fluxes	30 min (0.03 s)	4

properties. It is dopplerised and dual-polarised, but transmits horizontally polarised radiation only and detects horizontally and vertically polarised reflections providing the linear depolarisation ratio (LDR) of the hydrometeors. With a 200 ns pulse duration and a 0.7° beam width, it reaches a very fine spatial resolution of 30 m for radial velocity. Additional data measured in the absence of clouds are available to determine radial velocity when clear-air returns are sufficient (e.g. caused by insects or other floating material/debris, dust and Bragg scattering

Table 1b: Measurement systems included in KITcube and main derived parameters, typical settings, and measurement ranges of instruments. The measurement range column includes the minimal distance, spatial resolution, and maximum distance. x stands for a variable resolution.

Device (Manufacturer)	Quantity	Derived parameters	Temporal resolution of derived parameters (raw data)	Measurement range (m)
		Mean and turbulent atmospheric conditions		
Radiosonde system (Graw)	2	Temperature	2–8* (1 s)	0:x:15000
		Humidity	2–8* (1 s)	0:x:15000
		Wind velocity and direction	2-8* (1 s)	0:x:l5000
Microwave radiometer (Radiometer Physics)	1	Temperature	10 s	0:50:1200, 1200:200:5000, 5000:400:10000
		Humidity	10 s	0:200:2000, 2000:400:5000, 5000:800:10000
		IWV	10 s	–
		LWP	10 s	–
		Infrared temperature	10 s	–
GPS receiver (JAVAD)	1	IWV	15 min	–
Sodar (Scintec)	1	Wind velocity and direction	30 min	30:10:1000
		Vertical velocity variance	30 min	30:10:1000
Wind lidar, WindTracer (Lockheed Martin)	2	Radial velocity	0.1–1 s	375:x:12000
		Aerosol backscatter	0.1–1 s	375:x:12000
		Wind velocity and direction	scan dependent	75:50:8475
Wind lidar, Windcube (Leosphere)	1	Radial velocity	1.6 s	40:20:600
		Wind speed and direction	10 min (7 s)	40:20:600
		Measurements of clouds and precipitation properties		
Cloud camera (Mobotix)	2	Hemispheric photo	2 min	–
Cloud radar (Metek)	1	Radial velocity	1–10 s	150:30:14460
Ceilometer (Jenoptik)	1	Cloud base heights	1 min	150:15:15000
X-band radar (Gematronik)	1	Precipitation	5 min	125:250:100000
Micro rain radar (Metek)	1	Precipitation, Drop size distribution	1 min, 1 min	100:100:3200, 100:100:3200
Disdrometer (KIT)	1	Precipitation, Drop size distribution	1 min, 1 min	1, 1
Disdrometer (Distromet)	1	Precipitation, Drop size distribution	1 min, 1 min	0.1, 0.1
Rain gauge (EML)	2	Precipitation	1 min	1

*height dependent

from refractive-index fluctuations; BANTA et al., 2013). The cloud radar is able to scan at all azimuths from vertical direction down to the 45° zenith angle. Typically, a time resolution of 10 s is used in the vertical stare mode. Additional instrument specifications are given by TRÄUMNER et al. (2011).

To measure the cloud base height (CBH), the cloud radar is complemented by a ceilometer (CHM15k, Jenoptik). The ceilometer is a lidar providing uncalibrated backscatter at a spatial resolution of 15 m. From these raw data, CBHs, intrusion depths, and other properties of up to three different cloud layers can be determined.

Volume filling information on precipitation is gathered by a mobile X-band radar (Meteor 50DX, Gematronik). This radar is dopplerised and able to measure polarisation properties of the hydrometeors. It transmits radiation polarised at 45°, whereas the received signals are split up into the horizontal and vertical polarisation, thus providing polarisation properties, such as differential reflectivity (ZDR) and specific differential phase (KDP).

The transmitted peak power is roughly 70 kW and the beamwidth is 1.3°. Pulse widths between 0.5 μs and 2 μs lead to spatial resolutions down to 75 m. The radar reaches the total upper half-space down to an elevation of -2°. The horizontal range of the radar is about 100 km.

A Micro rain radar (MRR2, Metek) measures drop size distributions at 30 different heights with a layer spacing of up to 200 m. Mostly, this device is operated with a layer spacing of 100 m and a temporal resolution of 1 min. This radar (mean power 50 mW, 3° beam width, frequency 24 GHz) measures the reflected power as a function of the Doppler shift. Assuming negligible vertical air motion, the drop size distribution is determined in each layer for droplets between 0.2 mm and 6 mm in diameter.

An optical disdrometer (Parsivel, KIT) and a mechanical disdrometer (Joss-Waldvogel, Distromet) as well as a tipping bucket rain gauge (EML) complete the equipment used for in-situ precipitation measurements. All these devices have a temporal resolution of 1 min.

2.4 The KITcube control centre

To fully use the synergetic effects of the different instruments for process studies and to guarantee a high level of data quality and security, a sophisticated instrument and data management is implemented. The control centre of the KITcube, housed in a swap body (EN 284), collects all the data from the different instruments either via optical fibres, WLAN, or satellite transmission so that the data are available in near real-time. The control centre allows for a coordinated scan strategy to ensure simultaneous monitoring of the different scanning instruments in the same direction or volume: e.g. combined range height indicator (RHI) scans or PPI scans with the two lidars, microwave radiometer and cloud radar in or perpendicular to the prevailing wind direction; or observations in the vertical stare mode to investigate CBL features like up- and downdraughts and related turbulent characteristics like profiles of the vertical velocity variance in the CBL.

To ensure a high data availability, online monitoring of the states of the instruments (alert indication) is implemented in KITcube, which allows the operator in the control centre to react immediately to instrument failures. The collected data are archived on a data file server and stored in an additional database which is connected to a graphic user interface, the so-called advanced data extraction infrastructure (ADEI). ADEI does not only serve as a graphic interface, but also allows for exporting data in different file formats. To guarantee a high level of data security, the data are stored on a back-up server and mirrored on the main KITcube file server at KIT in Karlsruhe.

3 KITcube deployment during HyMeX

The aims of KITcube during HyMeX were twofold, i.e. (i) to allow for the investigation of convection initiated or modified by the Corsican Island and (ii) to provide the upstream conditions for most of the intense precipitation cases affecting continental south-eastern France and northern and central Italy. To reach these goals, the following configuration was selected: two main deployment sites were chosen, namely, the KITcube control centre at Corté (369 m MSL) in the Tavignano valley in the centre of Corsica and a site on the east coast (San Giuliano, 39 m MSL) (Fig. 1). The instrumentation deployed at both sites is listed in Table 2. The Corté site was equipped to capture the atmospheric conditions and evolution of moist convection in the centre of the island and the San Giuliano site was set up to cover coastal to maritime atmospheric conditions.

Table 2: Observation systems of KITcube deployed at the two main sites on the Corsican Island

Corté 43.30° N, 09.17° E, 369 m MSL	San Giuliano 42.27° N, 09.52° E, 39 m MSL
Energy balance station	Energy balance station
2 flux stations	2 flux stations
20-m tower	
Scintillometer	
Radiosonde system	Radiosonde system
Microwave radiometer	Microwave radiometer
GPS receiver	
	Sodar
Doppler wind lidar (WindTracer)	
Doppler wind lidar (Windcube)	
Cloud radar	
Ceilometer	
Cloud camera	Cloud camera
Disdrometers	
Micro rain radar	
Rain gauge	Rain gauge
	X-band radar

In order to determine the propagation speed of the sea breeze front in the Tavignano valley, one of the main valleys draining into the centre of Corsica, three mobile towers (Aléria, Casaperta, Pont Génois) were installed between the coast and Corté (Fig. 1).

Five additional JAVAD GPS receivers, including meteorological surface stations (wind, temperature, humidity, air pressure), were distributed in the KITcube area by GFZ Potsdam at Vergio, Rusio, La Porta, Bravone, and San Giuliano (Fig. 1) to enhance the spatial resolution of the existing GPS network operated by the Institut Geographique National (IGN) and ACTIPLAN company.

Finally, the Dornier 128 aircraft, D-IBUF, from TU Braunschweig, which is equipped with in-situ sensors for standard meteorological variables and turbulence (CORSMEIER et al., 2001), was stationed at Solenzara (Fig. 1). It was operated on specific IOP days to measure wind, temperature, and humidity profiles in the west and

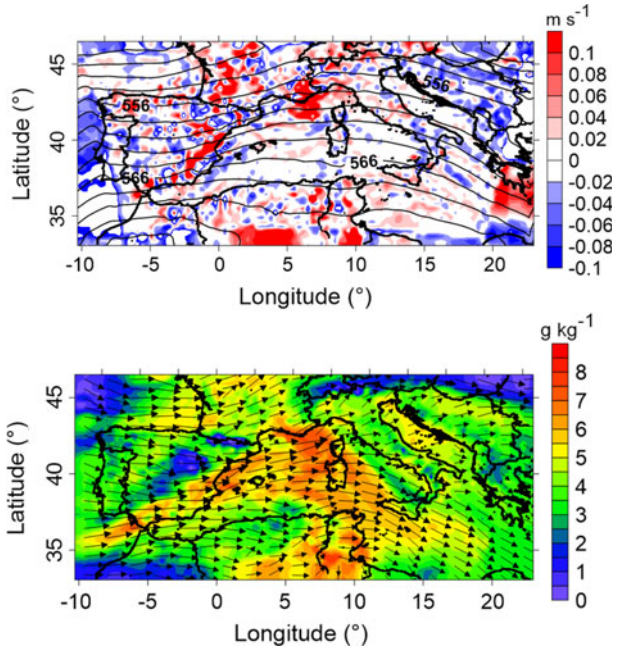

Figure 2: (a) COSMO-EU analysis of 500 hPa geopotential height in gpdm (isolines) and vertical velocity (colour-coded) and (b) specific humidity (colour-coded) and horizontal wind vectors at 700 hPa level on 11 October at 1200 UTC.

east of Corsica; conditions along east-west flight tracks across the island; and momentum, heat, and moisture fluxes over the sea.

4 Observations by KITcube from IOP 12

The IOP 12 of HyMeX (from 11 to 12 October) included days when Catalonia, Corsica, Tuscany, and central Italy were affected by heavy thunderstorms with precipitation (DUCROCQ et al., 2013). A period from IOP 12a (11 October) is analysed in the following.

4.1 Synoptic conditions

In the morning of 11 October, Corsica was ahead of a smooth trough (Fig. 2a). The trough axis and the associated surface low passed the island during the subsequent night. The passage of the inherent cold front was associated with embedded thunderstorm cells and heavy precipitation. Ahead of the trough, moist air was transported eastwards with the large-scale westerly flow (Fig. 2b). Around noontime, convection indices derived from radiosounding data indicated low convective instability and hardly any convective inhibition. At 500 hPa, however, large-scale weak lifting was present (Fig. 2a) and favoured convection. In the moist air mass, convective precipitating cells developed over Corsica between 1000 UTC and 1800 UTC, while more stratiform precipitation prevailed over the sea (Fig. 3). The evolution of the boundary layer conditions, thermally-induced circulation systems, and prefrontal precipitating cells over the island on this day could be investigated in detail with KITcube.

4.2 Conditions on the Corsican Island

Over Corsica, spatially different atmospheric conditions developed in the morning. At San Giuliano on the east coast, the day began cloud-free so that global radiation at about 0830 UTC reached up to 500 W m^{-2} (Fig. 4). Consequently, due to the onset of the sensible and latent heat flux, temperature and specific humidity increased after 0600 UTC and at 0830 UTC reached about 23 °C and 12 g kg^{-1}, respectively. Caused by the land-sea temperature contrast, the north-westerly nocturnal land breeze was replaced by southerly to south-easterly winds at about 0800 UTC. At Rusio, a station on a north-eastwards exposed slope (Fig. 1), weak slope winds set in at 0600 UTC already, i.e. right after the temperature increased (Fig. 4).

At Corté, some passing upper-level clouds caused a reduced radiation between 0600 and 0800 UTC already (Fig. 5). Until about 0840 UTC, the global radiation increased and reached up to 450 W m^{-2}. Between sunrise and 0840 UTC, the temperature increased by about 8 °C and reached 18 °C. This resulted in the onset of a moderate south-easterly upvalley wind at 0800 UTC. All three thermally driven wind systems – sea breeze, slope wind, and upvalley wind – persisted at least until the first precipitation occurred after 1000 UTC (Fig. 4 and 5).

From radiosondes and remote sensing data, the depths of the different wind systems were deduced. At San Giuliano, a south-easterly wind extended up to about 500 m AGL and a more southerly wind prevailed above up to a height of 1300 m AGL at 0900 UTC (Fig. 6a). Above this layer, a large-scale westerly flow was found. At around 1400 UTC, when a precipitation system occurred above the north-eastern part of Corsica (Fig. 3), the westerly flow temporary penetrated down to the ground.

At Corté, three wind layers were present at 0700 UTC – a weak downvalley wind of about 200 m depth, an elevated easterly flow between 300 m and 700 m AGL, and the westerly large-scale flow above (Fig. 6b). The origin of the elevated easterly flow could not be explained by the KITcube observations, but was probably part of a low-level large-scale flow around the Corsican Island, as was suggested by the analysis of the synoptic data. After the onset of the upvalley wind, the coupled upvalley wind and the elevated easterly flow led to a south-easterly flow of 1000 m depth. These two layers persisted until

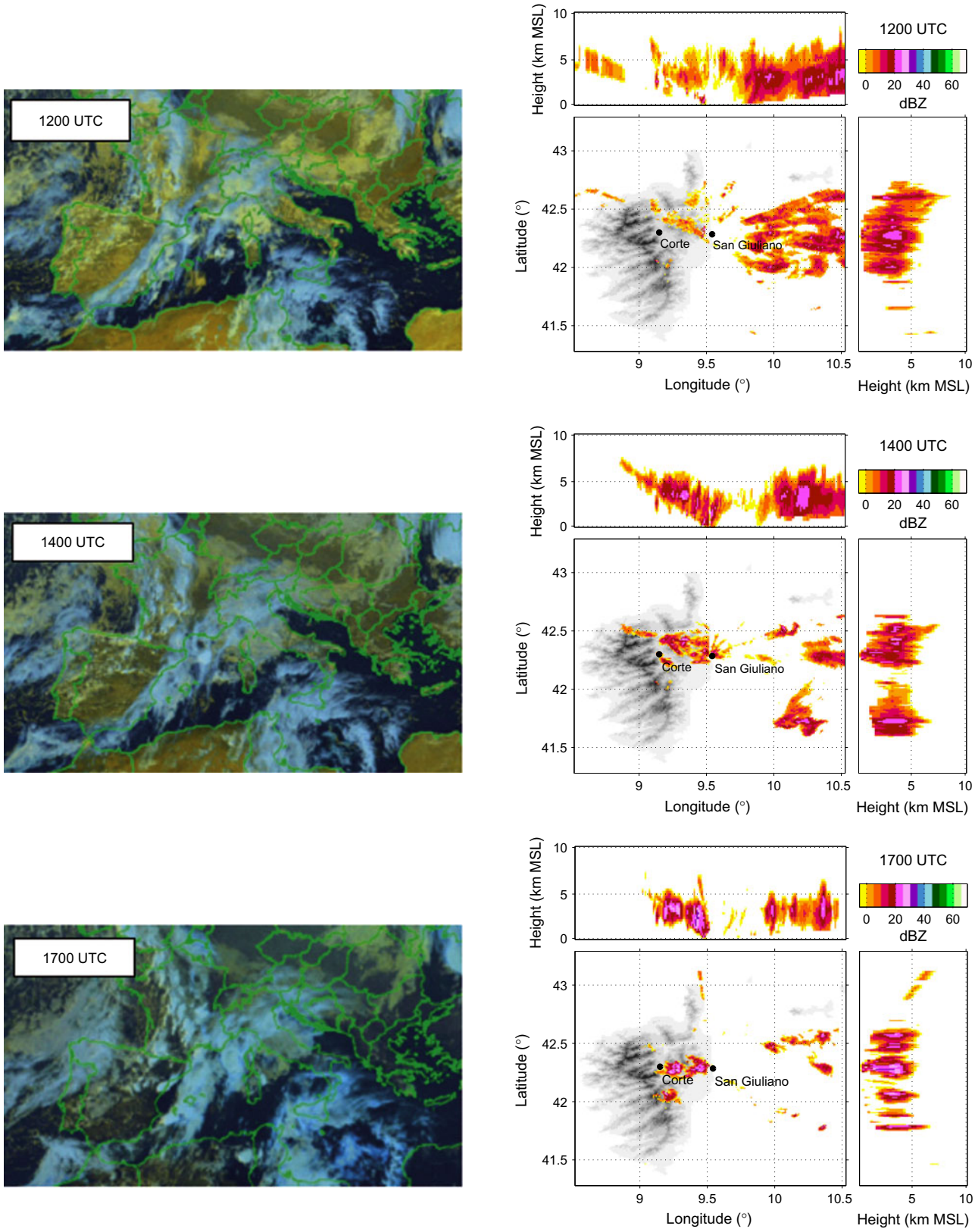

Figure 3: (left) Cloud composites (MeteoFrance) and (right) maximum constant altitude plan position indicator (MAX-CAPPI) of radar reflectivity on 11 October at 1200 UTC, 1400 UTC, and 1700 UTC (top to bottom).

about 1400 UTC when, associated with convective showers, westerly wind replaced the upvalley wind, while the elevated easterly flow below the clouds still remained (Fig. 5 and 6b). The different wind layers were also found in the wind lidar data when applying the VAD algorithm for horizontal wind field calculation (not shown).

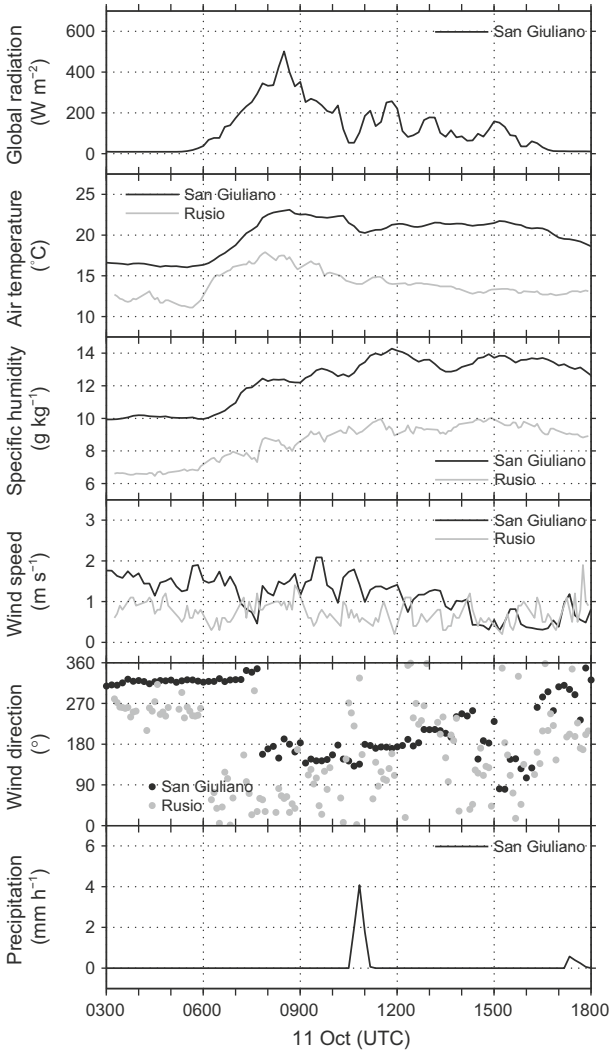

Figure 4: Global radiation and precipitation at San Giuliano and temperature, specific humidity, horizontal wind speed, and wind direction at San Giuliano and Rusio on 11 October.

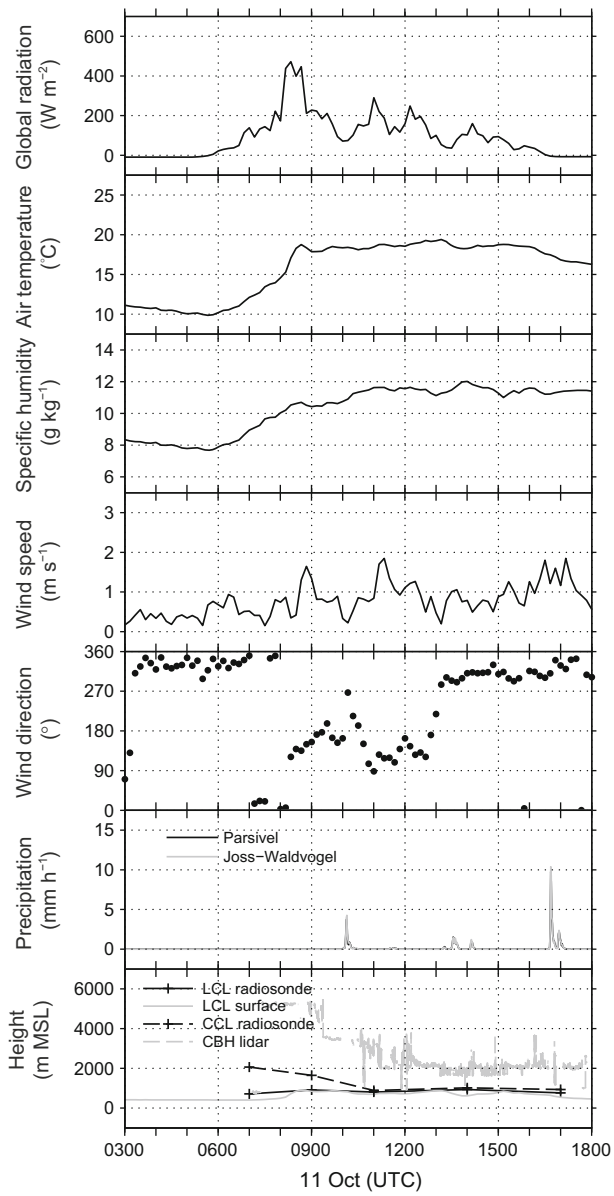

Figure 5: Global radiation, temperature, specific humidity, horizontal wind speed, and wind direction, precipitation, LCL, CCL, and CBH at Corté on 11 October.

Fig. 7 presents the combination of cloud radar, radiosonde, ceilometer, and wind lidar data for the Corté site. High specific humidity values (> 8 g kg^{-1}) were found in the layer of the upvalley wind and elevated easterly flow (Fig. 7a). The spatial IWV distribution as measured by the scanning microwave radiometer indicated that the high humidity advected by these wind systems from the sea was transported further upwards by the slope winds to the mountain crests west of Corté (not shown). In the morning until about 1100 UTC, a significant humidity increase was found in a layer between 1 km and 3 km AGL (Fig. 7a), which was also present in the COSMO-EU analysis (Fig. 2). This humidity increase caused by large-scale advection contributed mainly to the strong increase of IWV in the morning (Fig. 8). The time series of IWV show that a first IWV maximum of more than 34 kg m^{-2} occurred on the western coast (Osani) at 1000 UTC, while in the centre (Corté) and on the eastern coast (Santa-Lucia-di-Moriani) a first peak was reached about one hour later.

When the air mass with higher humidity arrived, partly precipitating clouds formed. The cloud radar reflectivity data (Fig.7a) show that the convective clouds extended up to about 5 km to 6 km AGL. Between 0900 UTC and 1100 UTC, the CBH decreased from about 5 km to 1.7 km AGL. The CBH was determined from ceilometer data (Fig. 7b) and aerosol backscatter data of the wind lidar (detected using a threshold in aerosol backscatter of –7.2 dB) (Fig. 7c). The ceilometer data show several abrupt decreases in CBH e.g. at 1000 UTC, 1120 UTC, and 1300 UTC, which are not found in the CBH data from the wind lidar. Comparison with cloud radar reflectivity data (Fig. 7a) shows that this is due to the onset of rain and not caused by a change in CBH.

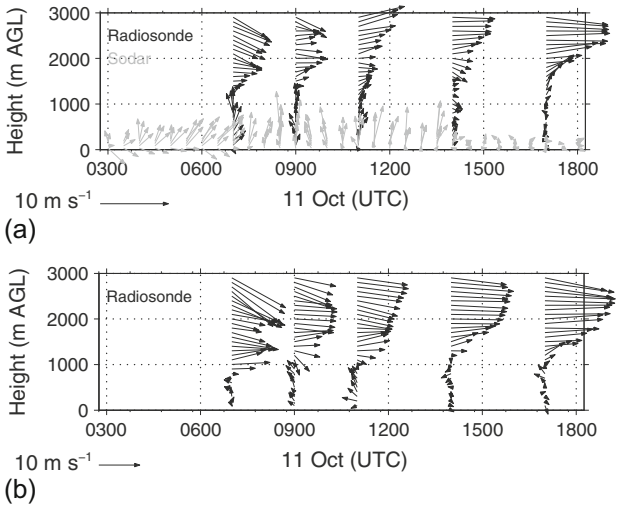

Figure 6: (a) Horizontal wind vectors derived from radiosondes (black) and sodar (grey) at San Giuliano and (b) horizontal wind vectors derived from radiosondes (black) at Corté on 11 October.

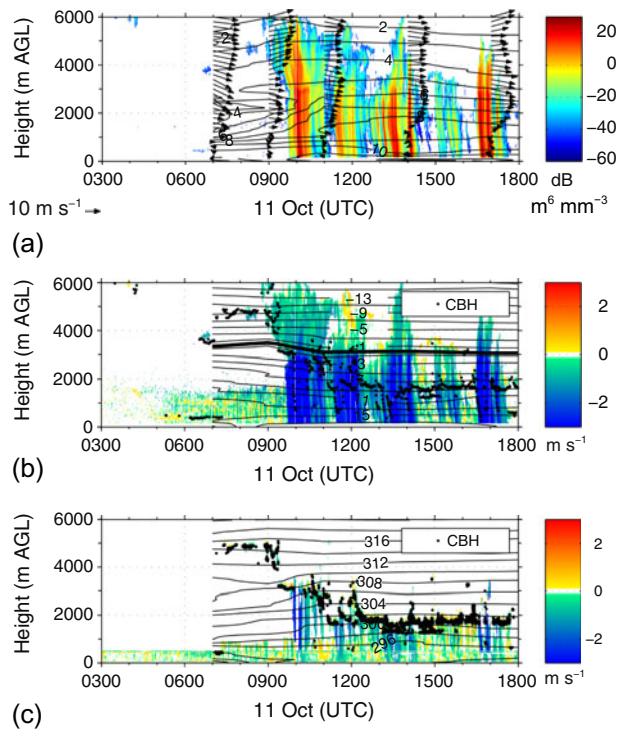

Figure 7: (a) Specific humidity (isolines), cloud radar reflectivity (colour-coded), and horizontal wind vectors (arrows); (b) temperature (isolines), vertical velocity (colour-coded), CBH (dotted), and 0° C level (thick solid line); and (c) potential temperature (isolines), vertical velocity (colour-coded), and CBH (dotted) at Corté on 11 October. Vertical velocity is calculated from cloud radar in (b) and wind lidar data in (c). CBH is determined from ceilometer in (b) and wind lidar data in (c). Temperature, specific humidity, and wind vectors are from radiosonde data.

Comparison of the observed CBH with CCL and LCL calculated from surface and radiosounding data at Corte (Fig. 5) shows that the observed CBH was much higher

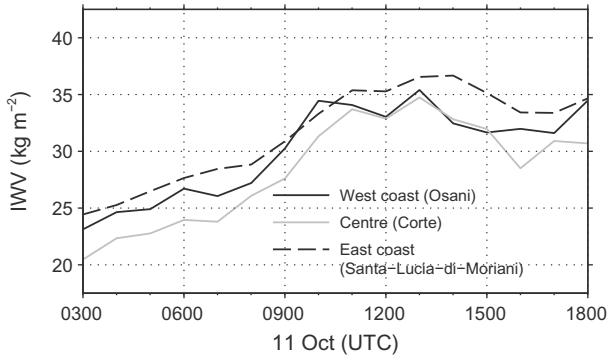

Figure 8: Time series of IWV from operational GPS stations on the west coast (Osani), in the centre (Corté), and on the east coast (Santa-Lucia-di-Moriani) of Corsica on 11 October.

than the LCL and CCL. On this day, the temperature in the upvalley wind layer and elevated easterly flow was stably stratified throughout the day (Fig. 7c) so that the convection temperature was not reached at the ground. This indicates that the clouds were not locally initiated, but orographically triggered over the mountain crests west of Corté and then transported eastwards with the large-scale westerly flow. This also corresponds to the rain radar measurements (Fig. 3): during four periods with precipitation between about 1000 UTC and 1800 UTC, the precipitating cells in the radar image for the first time appeared over the Corsican mountains.

The vertical velocity measured by the cloud radar showed some weak dry convective activity before 0930 UTC (Fig. 7b). During cloudy periods, precipitation could be identified apart from high reflectivity due to high values of negative vertical velocity of falling raindrops. The abrupt change in the vertical velocity from > -1 m s^{-1} to about -3 m s^{-1} at a height of about 3 km AGL marks the melting layer and separates falling snow above from raindrops below, as obvious from the comparison with the vertical temperature distribution (Fig. 7b). In the layers with rain, the vertical velocity of the ambient air could not be calculated. The cloud radar data showed that upward motion was encountered in a few areas in the clouds only – mainly at the cloud tops.

The vertical velocities, w, from the two wind lidars (WindTracer, Windcube) are combined in Fig. 7c. As already seen in the cloud radar data, weak dry convection was present in the morning before the first precipitation occurred. Below the precipitating clouds, the manufacturer's built-in dominant-peak algorithm calculated negative vertical velocity. To determine the velocity, a wind lidar measures the Doppler shift of the backscattered light induced by the particles in the atmosphere. The particles are considered to have no air speed, but to drift with the wind only. Typically, this results in a Gaussian-shaped peak in the Doppler spectrum, with a maximum at the most prevalent velocity (which is D^2-weighted) and a width characterising the turbulent condition. During special atmospheric events, like rain and snow fall or in

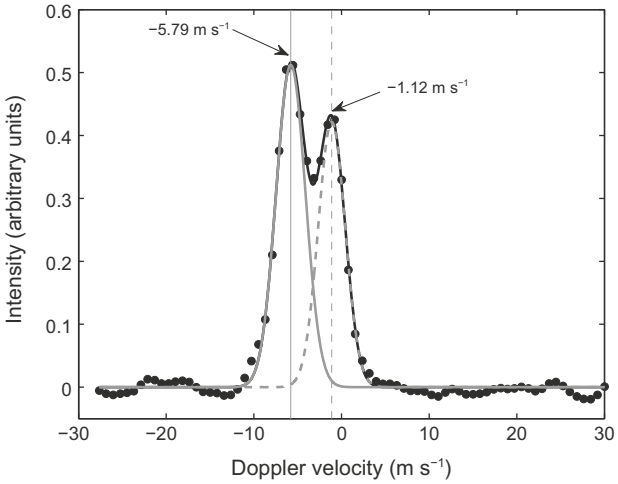

Figure 9: Doppler spectrum with double peak at the 3rd lidar range gate (466 m AGL) at Corté at 1005 UTC on 11 October. Solid and dashed grey lines mark the Gaussian double peaks derived from the Doppler vertical velocity distribution (black dots). For details see section 4.2.

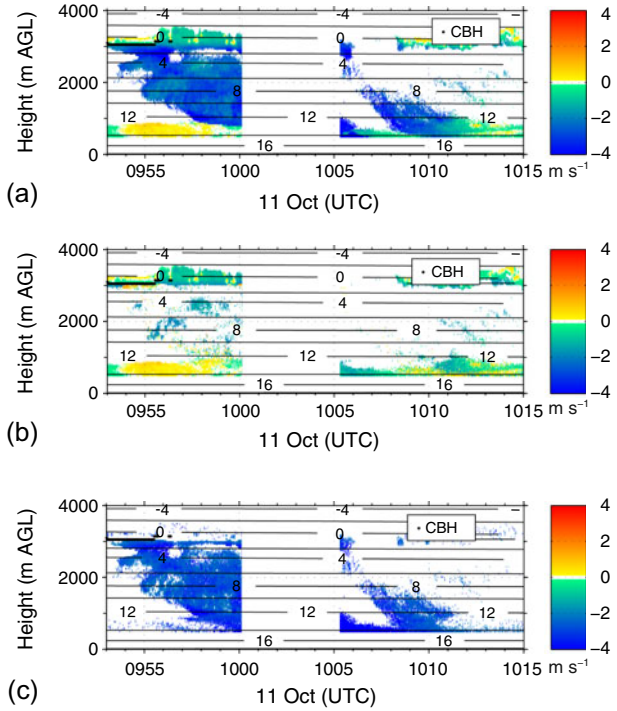

Figure 10: Rain episode as observed by Doppler wind lidar: (a) vertical velocity derived from the dominant peak in the Doppler spectrum; (b) vertical velocity derived from the peak classified as vertical velocity of the ambient air (heights <1000 m AGL), raindrops of smaller size (1000 m AGL < heights < 3000 m AGL), and droplets or snow (heights > 3000 m AGL); (c) vertical velocity derived from the peak classified as velocity of the falling raindrops at Corté on 11 October. Solid lines are temperature isolines from radiosoundings. CBH (dotted) is determined from wind lidar data. For details see section 4.2.

clouds, more than one velocity range may exist. In these cases, more than the dominant peak in the Doppler spectra may occur, as is illustrated by the example in Fig. 9. To account for this situation, a specially designed automatic algorithm was developed to distinguish between two potential peaks. A Gaussian-shaped double peak

$$I(w) = A_1 exp\left(-\left(\frac{w-\overline{w_1}}{\sigma_1}\right)^2\right) + A_2 exp\left(-\left(\frac{w-\overline{w_2}}{\sigma_2}\right)^2\right)$$

was fitted to the vertical velocity spectrum between -11.05 m s^{-1} and 12.6 m s^{-1} using a least-square-method. The parameter $A_{1,2}$ are the values of the intensities' peaks, $\overline{w_{1,2}}$, are the positions of the centers of the peaks, and the standard deviations, $\sigma_{1,2}$, control the widths of the two bell-shaped curves. This double peak-fit algorithm is quite sensitive to the used initial values. For this reason, a routine calculates different initial values. If the expected values of the two peaks are separated by less than 2 m s^{-1} or the width of at least one peak is narrower than 1 m s^{-1}, the algorithm uses a single-peak procedure again to determine only one velocity. The algorithm reproduces 98.5% of the velocities determined by the manufacturer's built-in dominant peak-finding algorithm. In about one third of all cases with an SNR ratio of more than -6 dB, a second considerable peak was determined by the double-peak algorithm.

On 11 October, two intensity peaks occurred in the clouds, in the aerosol layer, as well as in the aerosol-free layer in between. Fig. 10 presents the results for a shorter time period around 1000 UTC of the whole precipitation event (Fig. 7). The vertical velocity derived from the dominant peak in the Doppler spectrum is shown in Fig. 10a. In the clouds (CBH ≈ 3000 m AGL), the two peaks probably resulted from small cloud droplets or snow (Fig. 10b), and bigger, already falling raindrops (Fig. 10c). In the aerosol layer (< 1000 m AGL), one peak resulted from aerosols and, thus, represents the vertical velocity of the ambient air (Fig. 10b) whereas the second was from the falling raindrops (Fig. 10c). In the layer between the aerosol and the cloud layer one peak was caused by falling raindrops (Fig. 10c). It is more difficult to interpret the lower velocities (Fig. 10b); the results need further investigations. The skill of the double peak algorithm is particularly evident in the aerosol layer between 0955 UTC and 1000 UTC and 1005 UTC and 1015 UTC, where the velocity of the falling raindrops and the vertical velocity of the ambient air could be separated: while the vertical velocity of the raindrops was around -3 m s^{-1}, the velocity of the ambient air was around 0 m s^{-1}.

5 Discussion and conclusions

The KITcube was designed and constructed to investigate meso-γ processes related to convection initiation, cloud

formation, and precipitation. The system was applied first during the HyMeX field campaign in autumn 2012. To demonstrate KITcube's capability, a period from the intensive operation period 12a (11 October) was selected here. This period included orographically induced cloud formation and precipitation. The synergetic use of KITcube's different in-situ and remote sensing systems provides a comprehensive overview of the mesoscale meteorological phenomena on that day. It enables insight into processes from varying perspectives and allows for the verification of parameters derived from different observation systems. Main results from HyMeX IOP 12a are:

The vertically high-resolved observations provided an overview of the complex wind field consisting of thermally-induced circulations and large-scale flow. The measurements also revealed that the deep south-easterly flow at Corté was a combination of the upvalley wind and an elevated easterly flow (Fig. 6).

The combination of radiosonde, microwave radiometer, and GPS data proved that the strong increase of IWV was mainly caused by large-scale humidity transport from the west in a layer between 1 km and 3 km AGL. The cloud radar observations showed that the precipitating clouds formed in this moist westerly flow.

As regards CBH detection, a comparison of ceilometer and wind lidar data with infrared temperatures measured by the microwave radiometer and cloud radar reflectivity data proved that the CBH measured by the ceilometer was temporarily too low. The ceilometer detected the arrival of shower lines as CBH (Fig. 7b) and was expectedly unable to detect the correct CBH during precipitation events.

By comparing CCL and LCL values estimated from surface and radiosounding data with CBH, it was concluded that the clouds at Corté were not locally initiated, but orographically triggered over the mountain crests in the west and then advected to the east. This was confirmed by rain radar data which showed that the precipitating cells for the first time appeared over the Corsican mountains on the upwind side of Corté.

Comparison of the vertical measurement ranges of the cloud radar and wind lidars under cloud-free conditions showed that the heights were quite different, e.g. after the onset of the upvalley flow, but before the onset of the first precipitation (0800 UTC – 0930 UTC). The aerosol layer of about 1000 m depth, which was found in the lidar measurements, was clearly bound to the height of the coupled moist upvalley and elevated easterly flow (Fig. 7). Backscatter from cloud radar, however, reached up to about 1600 m AGL, i.e. into the large-scale westerly flow. Because of different wavelengths, the wind lidar and cloud radar saw different particles in cloud-free atmospheres and, thus, provided data in various layers. Additionally, the cloud radar requires a smaller concentration of scatterers to provide sufficient backscatter data.

Detailed analysis of the vertical velocity spectra from the wind lidar partly allowed for the determination of vertical velocities of different scatterers. In clouds, these are probably caused by co-existing falling raindrops and snow or cloud droplets. In aerosol layers during rain events, the vertical velocity of falling raindrops could be distinguished from the vertical velocity of the ambient air. In the layer between the aerosol and cloud layer, the two detected vertical velocities might be produced by two classes of falling raindrops. During the precipitation event around 1000 UTC, the raindrops sizes ranged from 0.4 mm to 3 mm (Fig. 11). However, it is not clear which threshold of drop size separates the two vertical velocity ranges. Vertical velocities of the falling raindrops calculated with the cloud radar resulted in higher values (compare Fig. 7b and c), which is due to the stronger weighting of raindrops with greater diameters (D^2-weighted).

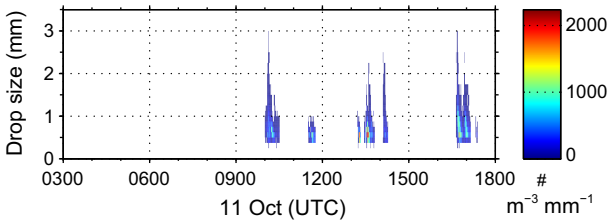

Figure 11: Drop size distribution measured with the Parsivel disdrometer at Corté on 11 October.

Apart from the mesoscale processes in Corsica, the KITcube data provided valuable information for the overall HyMeX goals, i.e. the analysis of high precipitation events over southern France and northern and central Italy. An additional benefit for the investigation of mesoscale processes results from supplementary Dornier 128 aircraft measurements during HyMeX (DUCROCQ et al., 2013). Several HyMeX dry and moist convection episodes are presently being investigated (e.g. ADLER and KALTHOFF, 2013; KALTHOFF and ADLER, 2013). They confirm KITcube's capability of analysing CBL-lower troposphere interactions on multiple scales.

Acknowledgments

This work is a contribution to the HyMeX programme. We would like to thank Veronique DUCROCQ from MeteoFrance and Evelyne RICHARD from the University of Toulouse/CNRS for their support in performing the measurements of KITcube on Corsica during HyMeX, Antoine PIERI from the fire brigade at Corté/University of Corsica and Olivier PAILLY from INRA in San Giuliano for their help and for hosting us during the nearly three-months' campaign. We are also grateful to the whole IMK team for their commitment to deploying the KITcube. The authors thank IGN and ACTIPLAN for operating the permanent GPS stations in Corté, Santa-Lucia-di-Moriani, and Osani, as well as IGN/SGN for processing these data operationally and

Olivier Bock (LAREG) for the screening of GPS data and conversion of ZTD into IWV using the methodology described in Bock et al. (2007). This work was also supported by the Atmospheric Observatory CORSICA (http://www.obs-mip.fr/). Finally, we acknowledge provision of cloud composites by MeteoFrance.

References

Adler, B., N. Kalthoff, 2013: Boundary-layer characteristics over complex terrain observed by remote-sensing systems during HyMeX. 32nd ICAM 2013. – Book of abstracts 5, Kranjska Gora, 3-7 June 2013.

Banta, R.M., 1990: The role of mountain flows in making clouds. In: Blumen, W.: Atmospheric processes over complex terrain. – Meteor. Monogr. **45**, 229–283.

Banta, R.M., C.M. Shun, D.C. Law, W.O. Brown, R.F. Reinking, R.M. Hardesty, C.J. Senff, M.J. Post, L.S. Darby, 2013: Observational techniques: Sampling the mountain atmosphere. – In: Mountain weather research and forecasting: Recent progress and current challenges, Chow, F.K., S.F. De Wekker, B.J. Snyder (Eds.). – Springer Atmospheric Sciences, Springer, 409–530, DOI: 10.1007/978-94-007-4098-3_8.

Behrendt, A., S. Pal, F. Aoshima, M. Bender, A. Blyth, U. Corsmeier, J. Cuesta, G. Dick, M. Dorninger, C. Flamant, P. Di Girolamo, T. Gorgas, Y. Huang, N. Kalthoff, S. Khodayar, H. Mannstein, K. Träumner, A. Wieser, V. Wulfmeyer, 2011: Observation of convection initiation processes with a suite of state-of-the-art research instruments during COPS IOP8b. – Quart. J. Roy. Meteor. Soc. **37**, 81–100.

Bock, O., M.-N. Bouin, A. Walpersdorf, J.-P. Lafore, S. Janicot, F. Guichard, A. Agusti-Panareda, 2007: Comparison of ground-based GPS precipitable water vapour to independent observations and numerical weather prediction model reanalyses over Africa. – Quart. J. Roy. Meteor. Soc. **133**, 2011–2027. doi: 10.1002/qj.185.

Browning, K.A., R. Wexler, 1968: The determination of kinematic properties of a wind field using Doppler radar. – J. Appl. Meteor. **7**, 105–113.

Browning, K., A. Blyth, P. Clark, U. Corsmeier, C. Morcrette, J. Agnew, D. Bamber, C. Barthlott, L. Bennett, K. Beswick, M. Bitter, K. Bozier, B. Brooks, C. Collier, C. Cook, F. Davies, B. Deny, T. Feuerle, R. Forbes, C. Gaffard, M. Gray, R. Hankers, T. Hewison, N. Kalthoff, S. Khodayar, M. Kohler, C. Kottmeier, S. Kraut, M. Kunz, D. Ladd, J. Lenfant, J. Marsham, J. McGregor, J. Nicol, E. Norton, D. Parker, F. Perry, M. Ramatschi, H. Ricketts, N. Roberts, A. Russell, H. Schulz, E. Slack, G. Vaughan, J. Waight, R. Watson, A. Webb, A. Wieser, 2007: The convective storm initiation project. – Bull. Amer. Meteor. Soc. **88**, 1939–1955.

Bryan, G.H., J.C. Wyngaard, J.M. Fritsch, 2003: Resolution requirements for the simulation of deep moist convection. – Mon. Wea. Rev. **131**, 2394–2416.

Buzzi, A., L. Foschini, 2000: Mesoscale meteorological features associated with heavy precipitation in the Southern alpine region. – Meteor. Atmos. Phys. **72**, 131–146.

Corsmeier, U., R. Hankers, A. Wieser, 2001: Airborne turbulence measurements in the lower troposphere onboard the research aircraft Dornier 128–6, D-IBUF. – Meteorol. Z. **10**, 315–329.

Corsmeier, U., N. Kalthoff, C. Barthlott, F. Aoshima, A. Behrendt, P. DiGirolamo, M. Dorninger, J. Handwerker, C. Kottmeier, H. Mahlke, S. Mobbs, E. Norton, J. Wickert, V. Wulfmeyer, 2011: Processes driving deep convection over complex terrain: A multi-scale analysis of observations from COPS-IOP9c. – Quart. J. Roy. Meteor. Soc. **137**, 137–155.

Crewell, S., U. Löhnert, 2003: Accuracy of cloud liquid water path from ground-based microwave radiometry. Part II. Sensor accuracy and synergy. – Radio Sci. **38**, 8042. doi: 10.1029/2002RS002634.

Dick, G., G. Gendt, C. Reigber, 2001: First experience with near real-time water vapor estimation in a German GPS network. – J. Atmos. Sol.-Terr. Phys. **63**, 1295–1304.

Doswell, C., A.C. Ramis, R. Romero, S. Alonso, 1998: A diagnostic study of three heavy precipitation episodes in the western Mediterranean region. – Wea. Forecast. **13**, 102–124.

Drobinski, P., V. Ducrocq, P. Alpert, E. Anagnostou, K. Béranger, M. Borga, I. Braud, A. Chanzy, S. Davolio, G. Delrieu, C. Estournel, N. Filali Boubrahmi, J. Font, V. Grubisic, S. Gualdi, V. Homar, B. Ivancan-Picek, C. Kottmeier, V. Kotroni, K. Lagouvardos, P. Lionello, M.C. Llasat, W. Ludwig, C. Lutoff, A. Mariotti, E. Richard, R. Romero, R. Rotunno, O. Roussot, I. Ruin, S. Somot, I. Taupier-Letage, J. Tintore, R. Uijlenhoet, H. Wernli, 2014: HyMeX, a 10-year multidisciplinary program on the Mediterranean water cycle. – Bull. Amer. Meteor. Soc. doi: 10.1175/BAMS-D-12-00242.1.

Ducrocq, V., O. Nuissier, D. Ricard, C. Lebeaupin, S. Anquetin, 2008: A numerical study of three catastrophic precipitating events over southern France. II: Mesoscale triggering and stationarity factors. – Quart. J. R. Meteor. Soc. **134**, 131–145.

Ducrocq, V., I. Braud, S. Davolio, R. Ferretti, C. Flamant, A. Jansa, N. Kalthoff, E. Richard, I. Taupier-Letage, P.-A. Ayral, S. Belamari, A. Berne, M. Borga, B. Boudevillain, O. Bock, J.-L. Boichard, M.-N. Bouin, O. Bousquet, C. Bouvier, J. Chiggiato, D. Cimini, U. Corsmeier, L. Coppola, P. Cocquerez, E. Defer, J. Delanoë, P. Di Girolamo, A. Doerenbecher, P. Drobinski, Y. Dufournet, N. Fourrié, J.J. Gourley, L. Labatut, D. Lambert, J. Le Coz, F.S. Marzano, G. Molinié, A. Montani, G. Nord, M. Nuret, K. Ramage, B. Rison, O. Roussot, F. Said, A. Schwarzenboeck, P. Testor, J. van Baelen, B. Vincendon, M. Aran, J. Tamayo, submitted: HyMeX-SOP1, the field campaign dedicated to heavy precipitation and flash flooding in the northwestern Mediterranean. – Bull. Amer. Meteor. Soc. doi: 10.1175/BAMS-D-12-00244.1.

GENDT, G., G. DICK, C. REIGBER, M. TOMASSINI, Y. LIU, M. RAMATSCHI, 2004: Near real time GPS water vapor monitoring for numerical weather prediction in Germany. – J. Meteor. Soc. Japan. **82**, 361–370.

HOMAR, V., C. RAMIS, R. ROMERO, S. ALONSO, J.A. GARCIA-MOYA, M. ALARCON, 1999: A case of convection development over the Western Mediterranean Sea: a study through numerical simulations. – Meteor. Atmos. Sci. **71**, 169–188.

KALTHOFF, N., B. ADLER, 2013: Dependency of convection on environmental conditions over complex terrain during HyMeX. – 32nd ICAM 2013, Book of abstracts **46**, Kranjska Gora, 3–7 June 2013.

KALTHOFF, N., M. FIEBIG-WITTMAACK, C. MEIßNER, M. KOHLER, M. URIARTE, I. BISCHOFF-GAUß, E. GONZALES, 2006: The energy balance, evapo-transpiration, and nocturnal dew position of an arid valley in the Andes. – J. Arid Environ. **65**, 420–443. doi: 10.1016/j.jaridenv.2005.08.013.

KALTHOFF, N., B. ADLER, C. BARTHLOTT, U. CORSMEIER, S. MOBBS, S. CREWELL, K. TRÄUMNER, C. KOTTMEIER, A. WIESER, V. SMITH, P. DI GIROLAMO, 2009: The impact of convergence zones on the initiation of deep convection: A case study from COPS. – Atmos. Res. **93**, 680–694.

KALTHOFF, N., K. TRÄUMNER, B. ADLER, S. SPÄTH, A. BEHRENDT, A. WIESER, J. HANDWERKER, F. MADONNA, V. WULFMEYER, 2013: Dry and moist convection in the boundary layer over the Black Forest – a combined analysis of in situ and remote sensing data. – Meteorol. Z. **22**, 445–461. doi: 10.1127/0941-2948/2013/0417.

KHODAYAR, S., N. KALTHOFF, J. WICKERT, U. CORSMEIER, C.J. MORCRETTE, C. KOTTMEIER, 2010: The increase of spatial data resolution for the detection of the initiation of convection. A case study from CSIP. – Meteorol. Z. **19**, 179–198.

KHODAYAR, S., N. KALTHOFF, J. WICKERT, C. KOTTMEIER, M. DORNINGER, 2013: High-resolution representation of the mechanisms responsible for the initiation of isolated thunderstorms over flat and complex terrains: Analysis of CSIP and COPS cases. – Meteor. Atmos. Phys. **119**, 109–124.

KOTTMEIER, C., P. PALACIO-SESE, N. KALTHOFF, U. CORSMEIER, F. FIEDLER, 2000: Sea breezes and coastal jets in southeastern Spain. – Int. J. Climatol. **20**, 1791–1808.

KOTTMEIER, C., N. KALTHOFF, C. BARTHLOTT, U. CORSMEIER, J. VAN BAELEN, A. BEHRENDT, R. BEHRENDT, A. BLYTH, R. COULTER, S. CREWELL, P. DI GIROLAMO, M. DORNINGER, C. FLAMANT, T. FOKEN, M. HAGEN, C. HAUCK, H. HOLLER, H. KONOW, M. KUNZ, H. MAHLKE, S. MOBBS, E. RICHARD, R. STEINACKER, T. WECKWERTH, A. WIESER, 2008: Mechanisms initiating deep convection over complex terrain during COPS. – Meteorol. Z. **17**, 931–948. doi: 10.1127/0941-2948/2008/0348.

LAMBERT, D., M. MALLET, V. DUCROCQ, F. DULAC, F. GHEUSI, N. KALTHOFF, 2011: CORSiCA: a Mediterranean atmospheric and oceanographic observatory in Corsica within the framework of HyMeX and ChArMEx. – Advan. Geosci. **26**, 125–131.

LÖHNERT, U., S. CREWELL, 2003: Accuracy of cloud liquid water path from ground-based microwave radiometry. Part I. Dependency on cloud model statistics. – Radio Sci. **38**, 8041. doi: 10.1029/2002RS002654.

MAUDER, M., T. FOKEN, 2011: Documentation and instruction manual of the eddy covariance software package TK3. – Work Report University of Bayreuth, Dept. of Micrometeorology 46, University of Bayreuth, Bayreuth, ISSN 1614-8916, 58 pp.

MILLER, M.A., A. SLINGO, 2007: The ARM Mobile Facility and its first international deployment: Measuring radiative flux divergence in West Africa. – Bull. Amer. Meteor. Soc. **88**, 1229–1244.

QIAN, J.-H., 2007: Why precipitation is mostly concentrated over islands in the maritime continent. – J. Atmos. Sci. **65**, 1428–1441.

ROTUNNO, R., R. FERRETTI, 2001: Mechanisms of intense Alpine rainfall. – J. Atmos. Sci. **58**, 1732–1749.

STAWIARSKI, C., K. TRÄUMNER, C. KNIGGE, R. CALHOUN, 2013: Scopes and challenges of dual-Doppler lidar wind measurements – an error analysis. – J. Atmos. Ocean. Technol. **30**, 2044–2062. doi: 10.1175/JTECH-D-12-00244.1.

TAYLOR, C., D. PARKER, N. KALTHOFF, M.A. GAERTNER, N. PHILIPPON, S. BASTIN, P.P. HARRIS, A. BOONE, F. GUICHARD, A. AGUSTI-PANAREDA, M. BALDI, P. CERLINI, L. DESCROIX, H. DOUVILLE, C. FLAMANT, J.-Y. GRANDPEIX, J. POLCHER, 2011: New perspectives on land-atmosphere feedbacks from the African monsoon multidisciplinary analysis. – Atmos. Sci. Lett. **12**, 38–44.

TRÄUMNER, K., J. HANDWERKER, J. GRENZHÄUSER, A. WIESER, 2010: A synergy approach to estimate properties of raindrop size distributions using a Doppler lidar and cloud radar. – J. Atmos. Ocean. Technol. **27**, 1095–1100.

TRÄUMNER, K., C. KOTTMEIER, U. CORSMEIER, A. WIESER, 2011: Convective boundary-layer entrainment: short review and progress using Doppler lidar. – Bound.-Layer Meteor. **141**, 369–391.

WECKWERTH, T.M., 2000: The effect of small-scale moisture variability on thunderstorm initiation. – Mon. Wea. Rev. **128**, 4017–4030.

WECKWERTH, T.M., D.B. PARSONS, S.E. KOCH, J.A. MOORE, M.A. LEMONE, B.B. DEMOZ, C. FLAMANT, B. GEERTS, J. WANG, W.F. FELTZ, 2004: An overview of the international H2O project (IHOP_2002) and some preliminary highlights. – Bull. Amer. Meteor. Soc. **85**, 253–277.

WILSON, J.W., R.D. ROBERTS, 2006: Summary of convective storm initiation and evolution during IHOP: Observational and modeling perspective. – Mon. Wea. Rev. **134**, 23–47.

WILSON, J.W., R.E. CARBONE, J.D. TUTTLE, T.D. KEENAN, 2001: Tropical island convection in the absence of significant topography: Part II: Nowcasting storm evolution. – Mon. Wea. Rev. **129**, 1637–1655.

WULFMEYER, V., A. BEHRENDT, C. KOTTMEIER, U. CORSMEIER, C. BARTHLOTT, G.C. CRAIG, M. HAGEN, D. ALTHAUSEN, F. AOSHIMA, M. ARPAGAUS, H.-S. BAUER, L. BENNETT, A. BLYTH, C. BRANDAU, C.

CHAMPOLLION, S. CREWELL, G. DICK, P. DI GIROLAMO, M. DORNINGER, Y. DUFOURNET, R. EIGENMANN, R. ENGELMANN, C. FLAMANT, T. FOKEN, T. GORGAS, M. GRZESCHIK, J. HANDWERKER, C. HAUCK, H. HÖLLER, W. JUNKERMANN, N. KALTHOFF, C. KIEMLE, S. KLINK, M. KÖNIG, L. KRAUSS, C.N. LONG, F. MADONNA, S. MOBBS, B. NEININGER, S. PAL, G. PETERS, G. PIGEON, E. RICHARD, M.W. ROTACH, H. RUSSCHENBERG, T. SCHWITALLA, V. SMITH, R. STEINACKER, J. TRENTMANN, D.D. TURNER, J. VAN BAELEN, S. VOGT, H. VOLKERT, T. WECKWERTH, H. WERNLI, A. WIESER, M. WIRTH, 2011: The Convective and Orographically-induced Precipitation Study (COPS): the scientific strategy, the field phase, and research highlights. – Quart. J. Roy. Meteor. Soc. **137**, 3–30. doi: 10.1002/qj.752.